



Contents lists available at ScienceDirect

## Journal of Colloid and Interface Science

journal homepage: [www.elsevier.com/locate/jcis](http://www.elsevier.com/locate/jcis)

## Regular Article

# Nanowire-structured FeP-CoP arrays as highly active and stable bifunctional electrocatalyst synergistically promoting high-current overall water splitting



Hongbo Yu<sup>a</sup>, Luoluo Qi<sup>a</sup>, Yan Hu<sup>a</sup>, Yuan Qu<sup>a</sup>, Puxuan Yan<sup>a</sup>, Tayirjan Taylor Isimjan<sup>b,\*</sup>, Xiulin Yang<sup>a,\*</sup>

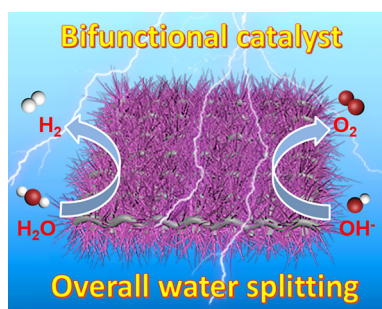
<sup>a</sup>Guangxi Key Laboratory of Low Carbon Energy Materials, School of Chemistry and Pharmaceutical Sciences, Guangxi Normal University, Guilin 541004, China

<sup>b</sup>Saudi Arabia Basic Industries Corporation (SABIC) at King Abdullah University of Science and Technology (KAUST), Thuwal 23955-6900, Saudi Arabia

## HIGHLIGHTS

- Fe<sub>0.14</sub>Co<sub>0.86</sub>-P/CC is fabricated by hydrothermal plus phosphating treatment.
- The catalyst exhibits excellent HER/OER performance in alkaline solution.
- The bifunctional catalyst only needs 1.95/2.14 V to reach 500/1000 mA cm<sup>-2</sup>.
- The synergy between FeP and CoP species dominates the excellent performance.

## GRAPHICAL ABSTRACT



## ARTICLE INFO

## Article history:

Received 11 March 2021

Revised 12 May 2021

Accepted 13 May 2021

Available online 18 May 2021

## Keywords:

Bimetal phosphide array

Electron-transfer

Bifunctional

Water splitting

Electrocatalysis

## ABSTRACT

The design and construction of highly efficient and durable non-noble metal bifunctional catalysts for oxygen evolution reaction (OER) and hydrogen evolution reaction (HER) in alkaline media is essential for developing the hydrogen economy. To achieve this goal, we have developed a bifunctional nanowire-structured FeP-CoP array catalyst on carbon cloth with uniform distribution through in-situ hydrothermal growth and phosphating treatment. The unique nanowire array structure and the strong electronic interaction between FeP and CoP species have been confirmed. Electrochemical studies have found that the designed Fe<sub>0.14</sub>Co<sub>0.86</sub>-P/CC catalyst appears excellent HER (130 mV@10 mA cm<sup>-2</sup>)/OER (270 mV@10 mA cm<sup>-2</sup>) activity and stability. Moreover, the bifunctional Fe<sub>0.14</sub>Co<sub>0.86</sub>-P/CC<sup>(+/-)</sup> catalyst is also used in simulated industrial water splitting system, where the pair catalyst requires about 1.95 and 2.14 V to reach 500 and 1000 mA cm<sup>-2</sup>, even superior to the control RuO<sub>2</sub><sup>(+)</sup>||Pt/C<sup>(-)</sup> catalyst, showing good industrial application prospects. These excellent electrocatalytic properties are attributed to the synergy between FeP and CoP species as well as the unique microstructure, which can accelerate charge transfer, expose more active sites and enhance electrolyte diffusion and gas emissions.

© 2021 Elsevier Inc. All rights reserved.

\* Corresponding authors.

E-mail addresses: [isimjant@sabic.com](mailto:isimjant@sabic.com) (T.T. Isimjan), [xlyang@gxnu.edu.cn](mailto:xlyang@gxnu.edu.cn) (X. Yang).

## 1. Introduction

Rapid development of society, the demand for energy supply and ecological environment quality is increasing [1]. However, energy supply is mainly dependent on fossil fuels, which not only have limited sources, but pollute the environment [2]. Therefore, it is urgent to find clean and renewable energy [3]. Currently, the

clean renewable energy conversion and storage systems developed by the society include fuel cells [4], metal-air cells [5], and electrochemical water splitting devices [6], etc. Among these systems, electrochemical water splitting devices are the best choice for the clean production of H<sub>2</sub> and O<sub>2</sub> [7,8]. However, the price of H<sub>2</sub> from electrolysis is more than five times higher than that of dry methane reforming. The two main factors that limit commercial application of the water electrolysis are price of the electricity and system efficiency. The system efficiency is mainly governed by the catalyst stability, hydrogen evolution reaction (HER), and oxygen evolution reaction (OER) efficiencies under high current density (>200 mA cm<sup>-2</sup>) and low over potentials (less than 100 mV). Because the slow oxygen evolution reaction (OER) kinetics involves a four-electron step, it requires high overpotential and high activation energy to overcome the complex oxidation process. To overcome this limitation, Wang et al. reported a series of transition metals (Fe and Mn) co-doped three-dimensional Ni<sub>3</sub>S<sub>2</sub>/NF via hydrothermal and sulfuration treatments. The resulting OER catalyst showed a low overpotential of 216 mV@30 mA cm<sup>-2</sup> [9]. Meanwhile, high overpotential and poor stability of hydrogen evolution reaction (HER) is also another bottleneck to be addressed. Therefore, it is urgent to develop OER and HER catalysts with excellent performance [10,11]. Up to now, the best OER (IrO<sub>2</sub>/RuO<sub>2</sub>) [12,13] and HER (Pt) [14] catalysts are based on noble metals. However, the high cost and scarcity of these precious metals limit their industrial application. Therefore, it is urgent to design and construct non-noble metal electrocatalysts with high OER and HER performance [15,16]. So far, a series of transition metal-based (TMB) catalysts with a good electrocatalytic performance, such as oxides [17,18], hydroxides [19,20], carbides [21,22], borides [23,24], phosphides [25,26], sulfides [27], and selenides [28,29], etc.

Transition metal-based bifunctional catalysts with low HER and OER overpotentials are particularly interesting, due to the simplicity of cell design and the possible capital cost reduction. However, it has its own challenges to overcome because the HER and OER follow different mechanisms, whereas the HER kinetics determined by chemisorption OH<sup>-</sup> and H<sup>\*</sup> and subsequent desorption of water molecule in an alkaline solution [30]. The recombination of two adsorbed H<sup>\*</sup> atoms is the rate determining step of HER [31]. Similarly, the OH<sup>-</sup> dissociation and surface intermediate (OH<sup>\*</sup>, OOH<sup>\*</sup>, and H<sup>+</sup>) chemisorption. Therefore, the catalysts that could bind with both hydrogen and oxygen containing intermediates are favored for overall water splitting. However, the reaction kinetics of two-electrode system is limited by the slow four-electron transfer kinetics of the OER that makes it even harder to design bifunctional water splitting catalyst [32,33].

The single transition metal phosphides in particular are often regarded as HER catalyst because the phosphorus and the metal atom cooperatively moderate the catalyst and hydrogen intermediate interaction thereof facilitate the hydrogen generation process [34]. Besides, the metal phosphates not only facilitate the metal atom oxidation by acting as proton acceptors, but induce distorted local metal geometry enhancing OER. Consequently, the bimetallic phosphide systems raised a lot of attention in the community [35]. For example, Yu et al. reported a bimetallic (Ni-Fe)P with optimized Ni/Fe ratio and high level of porosity that showed a low over potential both in HER and OER [36]. Tan et al. reported the nanoporous bimetallic (Co<sub>1-x</sub>Fe<sub>x</sub>)<sub>2</sub>P phosphides with controllable Co/Fe ratio and tunable porosity. The catalysts are prepared by electrochemical etching. The optimized catalyst exhibited versatile performance and low overpotential towards both HER and OER in an alkaline solution. Although they claim better performance than noble metal catalysts, the results were compared at a low current density [37].

Herein, we designed Fe-Co bimetallic phosphide nanowires on carbon cloth, which can directly undergo overall water splitting reaction. The bifunctional 3D catalyst arrays were prepared using a simple solvothermal approach followed by phosphatization with NaH<sub>2</sub>PO<sub>2</sub>. Because of the hierarchical nanostructures and synergistic effect between the FeP and CoP species, the optimized Fe<sub>0.14</sub>Co<sub>0.86</sub>-P/CC catalyst revealed comparable HER (130 mV@10 mA cm<sup>-2</sup>)/OER (270 mV@10 mA cm<sup>-2</sup>) activity and stability to the noble metal catalysts. Most importantly, the Fe<sub>0.14</sub>Co<sub>0.86</sub>-P/CC outperformed noble metal catalyst at industrial relevant high current density (>500 mA cm<sup>-2</sup>) two-electrode system with low cell voltages (1.97 V@500 mA cm<sup>-2</sup>, 2.14 V@1000 mA cm<sup>-2</sup>, and 2.31 V@1500 mA cm<sup>-2</sup>) and reasonable stability.

## 2. Experimental section

### 2.1. Synthesis of Fe<sub>x</sub>Co<sub>y</sub>-species on carbon cloth

All the chemicals used here are of analytical grade and used directly without further purification. The carbon cloth (CC, 1.5 cm × 4 cm) was ultrasonically cleaned with 1.0 M HCl, deionized water and ethanol for 10 min, and then repeated 3 times to remove impurities on the surface before further processing. The experimental details are the following: 0.7 mmol Fe(NO<sub>3</sub>)<sub>3</sub>·9H<sub>2</sub>O, 4.2 mmol Co(NO<sub>3</sub>)<sub>2</sub>·6H<sub>2</sub>O, 8.0 mmol CO(NH<sub>2</sub>)<sub>2</sub> and 3.2 mmol NH<sub>4</sub>F were dissolved in 70 mL ultra-pure water and 5 mL ethanol, and then stirred for 30 min to get a clear solution. The mixture was then transferred to a Teflon lined autoclave (100 mL) with a clean CC, heated to 140 °C at a heating rate of 5 °C min<sup>-1</sup>, and then kept for 10 h. After cooling to room temperature, the modified CC material was rinsed with ultra-pure water, ethanol for several times, and then dried in an oven at 60 °C for 2 h. According to the Fe/Co ratio (x/y), the resulting composite is named Fe<sub>x</sub>Co<sub>y</sub>-species/CC. A series of composite materials with different Fe/Co ratios were synthesized with the total amount of Fe<sup>3+</sup> and Co<sup>2+</sup> being 4.9 mmol, in which the molar ratios of Fe/Co were 1/0, 1/4, 1/8, and 0/1, respectively.

### 2.2. Synthesis of Fe<sub>x</sub>Co<sub>y</sub>-P/CC by vapor phase phosphidation

The phosphating process is carried out in a tube furnace, where 1.0 g of NaH<sub>2</sub>PO<sub>2</sub> is used as phosphorus source and placed in an upstream porcelain boat along with the precursor in another porcelain boat downstream. The furnace was heated to 350 °C with a heating rate of 5 °C min<sup>-1</sup> in N<sub>2</sub> atmosphere (20 sccm), and kept at 350 °C for 2 h. After phosphating treatment, the sample was cooled to ambient temperature in a flowing N<sub>2</sub> gas. After that, a series of samples were prepared using the similar method as discussed above, which were named as FeP/CC, Fe<sub>0.20</sub>Co<sub>0.80</sub>-P/CC, Fe<sub>0.11</sub>Co<sub>0.89</sub>-P/CC and CoP/CC, respectively.

For comparison, we also prepared RuO<sub>2</sub> and commercial Pt/C modified CC, of which 5.0 mg RuO<sub>2</sub> powder or commercial Pt/C (Johnson-Matthey) were dispersed in 480 μL deionized water, 480 μL absolute ethanol and 20 μL 5% Nafion to form a mixture solution. After sonication for 30 min, 200 μL of the slurry was pipetted onto a CC (1 cm × 1 cm) and dried at room temperature for later use.

### 2.3. Electrochemical measurements

An electrochemical workstation with a standard three-electrode system (Bio-Logic VMP3) was used to test the electrochemical performance of the designed catalyst in 1.0 M KOH electrolyte. Among them, the synthesized composite material, carbon rod, and saturated calomel electrode (SCE) are used as working,

counter, and reference electrodes, respectively. In the electrochemical test, we first used cyclic voltammetry (CV) for 3 ~ 5 consecutive tests to stabilize the performance of the catalyst with a scan rate of  $10 \text{ mV s}^{-1}$ . Second, the linear sweep voltammetry (LSV) was used to explore the catalytic performance of the catalyst for OER and HER at a sweep rate of  $2 \text{ mV s}^{-1}$ . Third, the electrochemical impedance spectroscopy (EIS) was tested near the onset potential in the frequency range of 200 kHz to 10 mHz. Finally, the stability of the catalyst was explored separately by chronopotentiometry. All those tests have been conducted *in situ* compensation and the potentials have been calibrated to standard hydrogen electrode (RHE). The calibration is obtained by using two clean Pt foils as working and counter electrodes in  $\text{H}_2$ -saturated 1.0 M KOH with a scan rate of  $5 \text{ mV s}^{-1}$ , the correction equation is  $E(\text{RHE}) = E(\text{SCE}) + 1.040 \text{ V}$  (Fig. S1).

The two-electrode industrial simulation test was conducted in a 30 wt% KOH solution with a scan rate of  $10 \text{ mV s}^{-1}$ . At the same time, a long-term stability test of the two-electrode bifunctional catalyst was also carried out at approximately  $25 \text{ }^\circ\text{C}$ .

### 3. Results and discussion

Fig. 1a is a schematic diagram of the synthesis of  $\text{Fe}_{0.14}\text{Co}_{0.86}\text{-P/CC}$  by a two-step method. In the first step, a certain amount of  $\text{Fe}(\text{NO}_3)_3 \cdot 9\text{H}_2\text{O}$ ,  $\text{Co}(\text{NO}_3)_2 \cdot 6\text{H}_2\text{O}$ , urea, and  $\text{NH}_4\text{F}$  are dissolved in  $\text{H}_2\text{O}$ -ethanol in an autoclave. As the temperature rises, urea will gradually decompose to create an alkaline environment, and the Fe and Co precursors therein can grow *in-situ* on CC surface in the presence of  $\text{NH}_4\text{F}$ . Next, the  $\text{PH}_3$  produced by the pyrolysis of  $\text{NaH}_2\text{PO}_2$  is used to phosphatize the precursor material in a tube furnace, thereby preparing  $\text{Fe}_{0.14}\text{Co}_{0.86}\text{-P/CC}$  composite materials. The mass of CC ( $1 \times 1 \text{ cm}^2$ ) loaded with catalysts and fresh CC were 14.5 mg and 13.4 mg, respectively. From this, we can conclude that the catalyst loading is  $1.1 \text{ mg cm}^{-2}$ . The ICP-AES test shows that the mass fractions of Fe and Co are 5.28% and 33.08% respectively, and the molar ratio is 1/6.15 in the  $\text{Fe}_{0.14}\text{Co}_{0.86}\text{-P/CC}$  composite (Table S1), which is consistent with the theoretical value.

To further study the crystal structure change of the catalytic material, we performed XRD analysis. Fig. 1b shows that the XRD patterns of the  $\text{Fe}_{0.14}\text{Co}_{0.86}$ -species prepared on the CC surface are mainly consistent with  $\text{Co}_3\text{O}_4$  (JCPDS: 43–1003) [38], and

$\text{FeOOH}$  (JCPDS: 34–1266) [39], along with a small amount of  $\text{CoFe}_2\text{O}_4$  (JCPDS: 22–1086). After phosphatization, the pure Fe species on the CC surface is subsequently converted to  $\text{FeP}$  (JCPDS: 39–0809) [40], and the pure Co species is phosphated to  $\text{CoP}$  (JCPDS: 29–0497) (Fig. S2) [41]. Notably, the  $\text{Fe}_{0.14}\text{Co}_{0.86}$ -species after phosphatization completely inherited in the crystal structure of  $\text{FeP}$  and  $\text{CoP}$  simultaneously in a hybrid structure (Fig. 1c). The specific surface area and porosity of the  $\text{Fe}_{0.14}\text{Co}_{0.86}\text{-P}$  composite (Scrape off the CC surface) are measured using a  $\text{N}_2$  adsorption-desorption isotherm test at 77 K. The results show that the Brunauer–Emmett–Teller (BET) surface area of the material is about  $27.8 \text{ m}^2 \text{ g}^{-1}$ , and the average pore size is *ca.* 18.1 nm through BJH method (Fig. S3). The larger BET surface area and porous characteristics increase the exposure of active sites, rapid electrolyte diffusion, and gas emission, thereby improving electrochemical activity.

The morphology and microstructure of the optimized catalyst were characterized by scanning electron microscopy (SEM) and transmission electron microscopy (TEM). As shown in Fig. S4, the surface of pristine CC is smooth initially and become the interwoven nanowire array-like structure after *in-situ* hydrothermal growth of  $\text{Fe}_{0.14}\text{Co}_{0.86}$ -species (Fig. S5). The nanowire array-like structure of  $\text{Fe}_{0.14}\text{Co}_{0.86}\text{-P}$  was preserved even after phosphatization (Fig. 2a). TEM was further used to explore the detailed morphology of  $\text{Fe}_{0.14}\text{Co}_{0.86}\text{-P}$  nanowires in nanoscale. As shown in Fig. 2b, the width of the nanowire is approximately 150 nm, and there are some particulate materials on the surface, which make the nanowire have a concave-convex structure, thereby exposing more reaction sites. The high-resolution TEM image shows two types of well-defined lattice fringes (Fig. 2c), one with a lattice spacing of 0.29 nm corresponds to the (020) crystal plane of orthorhombic  $\text{FeP}$ , and the other with lattice spacings of 0.19 nm and 0.24 nm attribute to the (202) and (102) crystal planes of orthorhombic  $\text{CoP}$ , respectively [42,43]. The selection electron diffraction (SAED) image shows a series of diffraction rings with dense bright spots (Fig. 2d) that represent the (020) and (230) crystal planes of  $\text{FeP}$ , and the (201) and (202) crystal planes of  $\text{CoP}$ . Furthermore, HAADF-STEM and the corresponding element mappings show that the elements of Fe, Co, and P are uniformly dispersed throughout the nanowire structure of  $\text{Fe}_{0.14}\text{Co}_{0.86}\text{-P}$  (Fig. 2e).

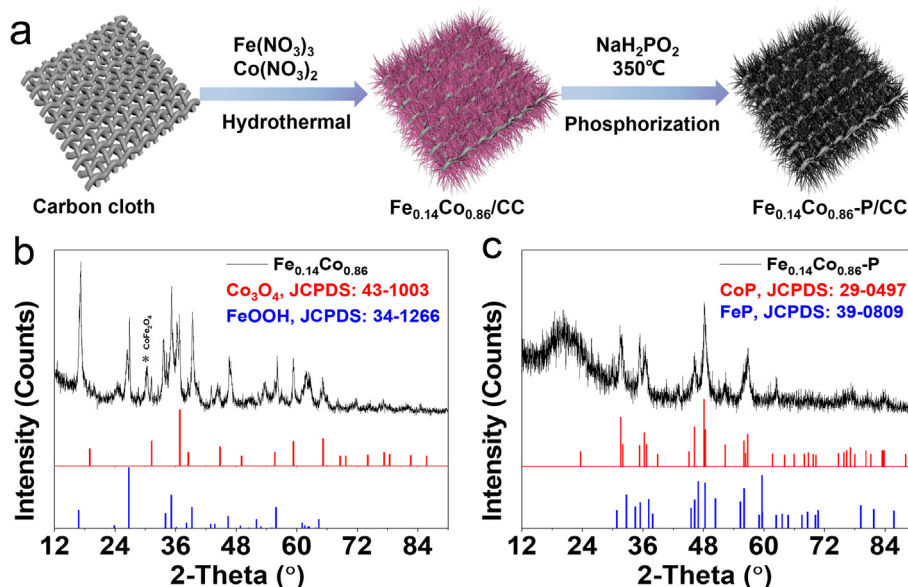
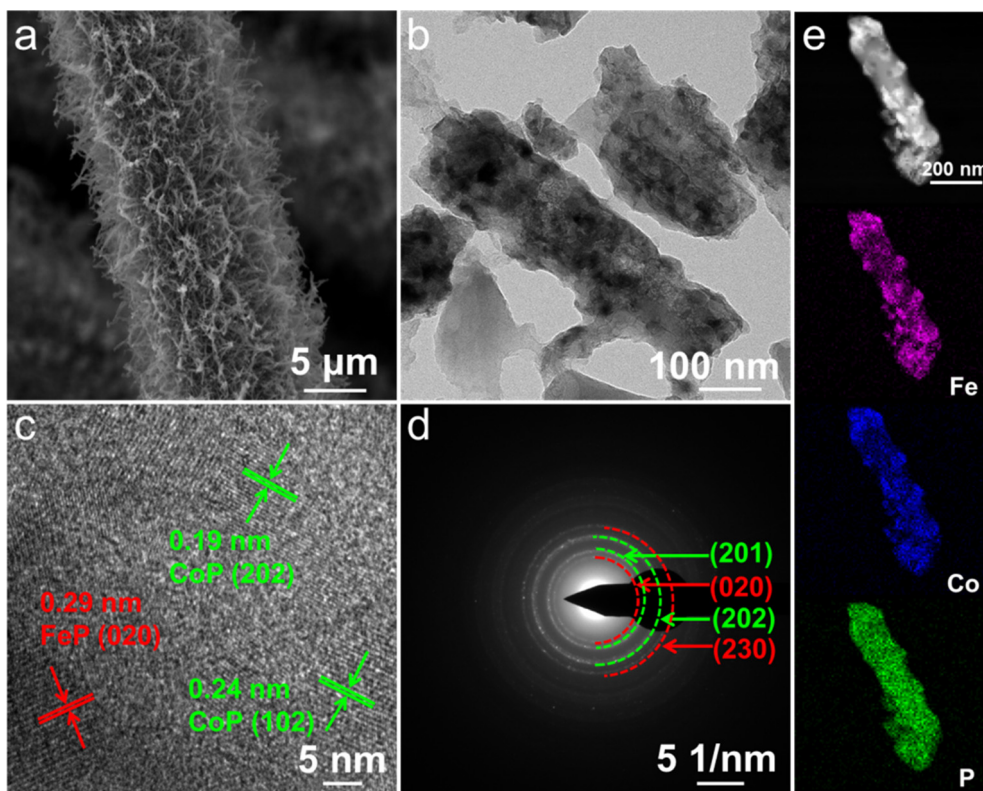


Fig. 1. (a) Schematic diagram of the formation of  $\text{Fe}_{0.14}\text{Co}_{0.86}\text{-P/CC}$  catalyst. (b) X-ray diffraction (XRD) patterns of  $\text{Fe}_{0.14}\text{Co}_{0.86}/\text{CC}$ . (c) X-ray diffraction (XRD) patterns of  $\text{Fe}_{0.14}\text{Co}_{0.86}\text{-P/CC}$ .



**Fig. 2.** SEM images of (a)  $\text{Fe}_{0.14}\text{Co}_{0.86}\text{-P/CC}$ , (b) TEM image and (c) high-resolution TEM image of  $\text{Fe}_{0.14}\text{Co}_{0.86}\text{-P/CC}$ . (d) SAED images of  $\text{Fe}_{0.14}\text{Co}_{0.86}\text{-P/CC}$ . (e) HAADF TEM image and elemental mappings of  $\text{Fe}_{0.14}\text{Co}_{0.86}\text{-P/CC}$ .

X-ray photoelectron spectroscopy (XPS) is used to explore the composition and chemical state of the composite. As shown in Fig. S6a, the  $\text{Fe}_{0.14}\text{Co}_{0.86}\text{-P/CC}$  material is composed of C, Fe, Co and P elements. The high-resolution XPS of C 1s was identified as C=C (284.0 eV), C—C (284.8 eV), C—O (286.0 eV) and C=O (288.0 eV) (Fig. S6b) [44], and was used as a calibration standard for other elements. As shown in Fig. 3a, the Fe  $2p_{3/2}$  region of  $\text{Fe}_{0.14}\text{Co}_{0.86}\text{-P/CC}$  is fitted with three peaks of FeP (707.2 eV), Fe-O

(711.4 eV) and one satellite peak (715.0 eV) [45,46]. Compared with FeP/CC, the binding energy of the Fe-P of  $\text{Fe}_{0.14}\text{Co}_{0.86}\text{-P/CC}$  is positively shifted by 0.35 eV. Moreover, the Co  $2p$  region of  $\text{Fe}_{0.14}\text{Co}_{0.86}\text{-P/CC}$  contains a pair of Co  $2p_{3/2}$  and Co  $2p_{1/2}$ , where the Co  $2p_{3/2}$  is fitted with three peaks of CoP (778.3 eV), CoO (781.6 eV) and a satellite (786.1 eV), respectively (Fig. 3b) [47]. As compare to CoP/CC, the Co-P binding energy of  $\text{Fe}_{0.14}\text{Co}_{0.86}\text{-P/CC}$  presented a negatively shifted of 0.31 eV. These phenomena indicate that

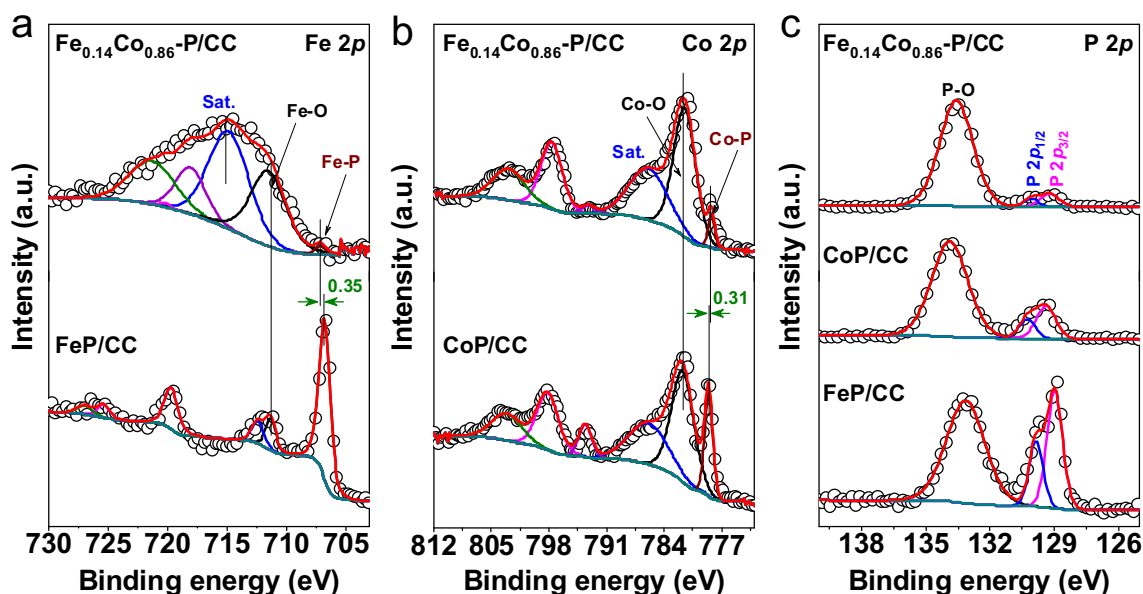


**Fig. 3.** High-resolution XPS spectra of (a) Fe  $2p$ , (b) Co  $2p$  and (c) P  $2p$  regions of  $\text{Fe}_{0.14}\text{Co}_{0.86}\text{-P/CC}$ , FeP/CC and CoP/CC, respectively.

there is a strong electronic interaction between FeP and CoP species in the  $\text{Fe}_{0.14}\text{Co}_{0.86}\text{-P/CC}$  composite [48]. Besides, the P 2p fitting of  $\text{Fe}_{0.14}\text{Co}_{0.86}\text{-P/CC}$  is shown in Fig. 3c, in which the high-resolution P 2p mainly was de-convoluted into two distinctive peaks as P  $2p_{3/2}$  (129.1 eV) and P  $2p_{1/2}$  (130.0 eV) for metal phosphates as well as an additional peaks for P–O bonds (133.6 eV) [40,49]. Moreover, we also compared the XPS before and after the stability test of the  $\text{Fe}_{0.14}\text{Co}_{0.86}\text{-P/CC}$  catalyst. The results show that part of the FeP and CoP species on the surface are oxidized to metal (oxy)hydroxide during the OER process (Figs. S6c–e) [35,50].

In order to evaluate the electrochemical performance of all catalysts, we first used LSV polarization curves to explore the changes in OER activity in 1.0 M KOH solution. The Fig. S7 shows the effect of different Fe/Co ratios on OER performance of  $\text{Fe}_x\text{Co}_y\text{-P/CC}$ . The  $\text{Fe}_{0.14}\text{Co}_{0.86}\text{-P/CC}$  revealed the best OER performance. If not specifically stated, the hybrid catalyst discussed below is  $\text{Fe}_{0.14}\text{Co}_{0.86}\text{-P/CC}$ . Furthermore, we employed the LSV polarization curve to explore the electrochemical performance of  $\text{Fe}_{0.14}\text{Co}_{0.86}\text{-P/CC}$ , along with FeP/CC, CoP/CC and  $\text{RuO}_2\text{/CC}$  with a scan rate of  $2\text{ mV s}^{-1}$ . Fig. 4a shows that  $\text{Fe}_{0.14}\text{Co}_{0.86}\text{-P/CC}$  catalyst only needs 270 mV to reach  $10\text{ mA cm}^{-2}$ , which is far lower than that of FeP/CC (456 mV), CoP/CC (334 mV), and close to  $\text{RuO}_2\text{/CC}$  (252 mV). It is worth noting that at a higher current density ( $>35\text{ mA cm}^{-2}$ ), the  $\text{Fe}_{0.14}\text{Co}_{0.86}\text{-P/CC}$  catalyst begins to outperform  $\text{RuO}_2\text{/CC}$ , showing a good industrial application prospect, which requires a stable performance at high current density at low overpotential. The superior electrocatalytic performance can be attributed to the synergy between the CoP and FeP components, which is also widely reported in the literature [51–53]. Previous DFT calculations also show that the Co-Fe-P hybrid composite can increase the density of states near the Fermi level [52], thereby increasing the inherent electrocatalytic activity.

To study the OER kinetics of different catalysts, the Tafel plots derived from the corresponding LSV curves were evaluated in Fig. 4b. The Tafel slope of  $\text{Fe}_{0.14}\text{Co}_{0.86}\text{-P/CC}$  catalyst is  $45.4\text{ mV}$

$\text{dec}^{-1}$ , which is significantly lower than those of FeP/CC ( $74.5\text{ mV dec}^{-1}$ ), CoP/CC ( $54.3\text{ mV dec}^{-1}$ ), and  $\text{RuO}_2\text{/CC}$  ( $61.1\text{ mV dec}^{-1}$ ). These results indicate that  $\text{Fe}_{0.14}\text{Co}_{0.86}\text{-P/CC}$  catalyst has the fastest reaction kinetics, thereof a favorable OER activity than other catalysts [54,55]. Moreover, it has outstanding OER activity than most recently reported metal phosphates with small Tafel slope and overpotential at  $10\text{ mA cm}^{-2}$  in alkaline medium (Fig. 4c, Table S2).

As shown in Fig. 4d, the double layer capacitance ( $C_{dl}$ ) value of  $\text{Fe}_{0.14}\text{Co}_{0.86}\text{-P/CC}$  is  $230.0\text{ mF cm}^{-2}$ , which is much larger than those of FeP/CC ( $52.1\text{ mF cm}^{-2}$ ), and CoP/CC ( $137.4\text{ mF cm}^{-2}$ ). The  $C_{dl}$  was calculated from the cyclic voltammetry (CV) curves at various scan rates in a non-Faradaic potential region (Fig. S8) [56]. In general, the superior OER electrocatalytic activity relates with the large electrochemical active surface area (ECSA). The double layer capacitance ( $C_{dl}$ ) is directly proportional to ECSA [17]. As shown in Fig. S9, the ECSA is calculated by  $\text{ECSA} = C_{dl}/C_s$ , where  $C_s$  is the average specific capacitance of  $0.04\text{ mF cm}^{-2}$  [55]. The ECSA of  $\text{Fe}_{0.14}\text{Co}_{0.86}\text{-P/CC}$  is  $5750\text{ cm}^2$ , which is much higher than these of CoP/CC ( $3435\text{ cm}^2$ ) and FeP/CC ( $1303\text{ cm}^2$ ), implying higher OER active sites density in  $\text{Fe}_{0.14}\text{Co}_{0.86}\text{-P/CC}$  [26].

The intrinsic catalytic activity per catalytic active site is estimated by the turnover frequency (TOF) value [57]. Fig. 4e shows the TOF curve at various overpotentials calculated using ICP metal contents from Table S1. As the overpotential increases, the TOF values of all catalysts increase monotonically. Among them, the  $\text{Fe}_{0.14}\text{Co}_{0.86}\text{-P/CC}$  catalyst shows the highest intrinsic catalytic activity once again confirmed the highest catalytic oxygen evolution conversion efficiency [18].

Electrochemical impedance spectroscopy (EIS) measurements were also performed to further understand the OER kinetics, and the corresponding results are shown in Fig. S10. The fitted charge transfer resistance ( $R_{ct}$ ) obtained from the semicircle is used to evaluate the electrocatalytic kinetics at the catalyst/electrolyte interface, where a low value corresponds to a fast electron transfer and a superior OER kinetics [54]. The  $\text{Fe}_{0.14}\text{Co}_{0.86}\text{-P/CC}$  presents the

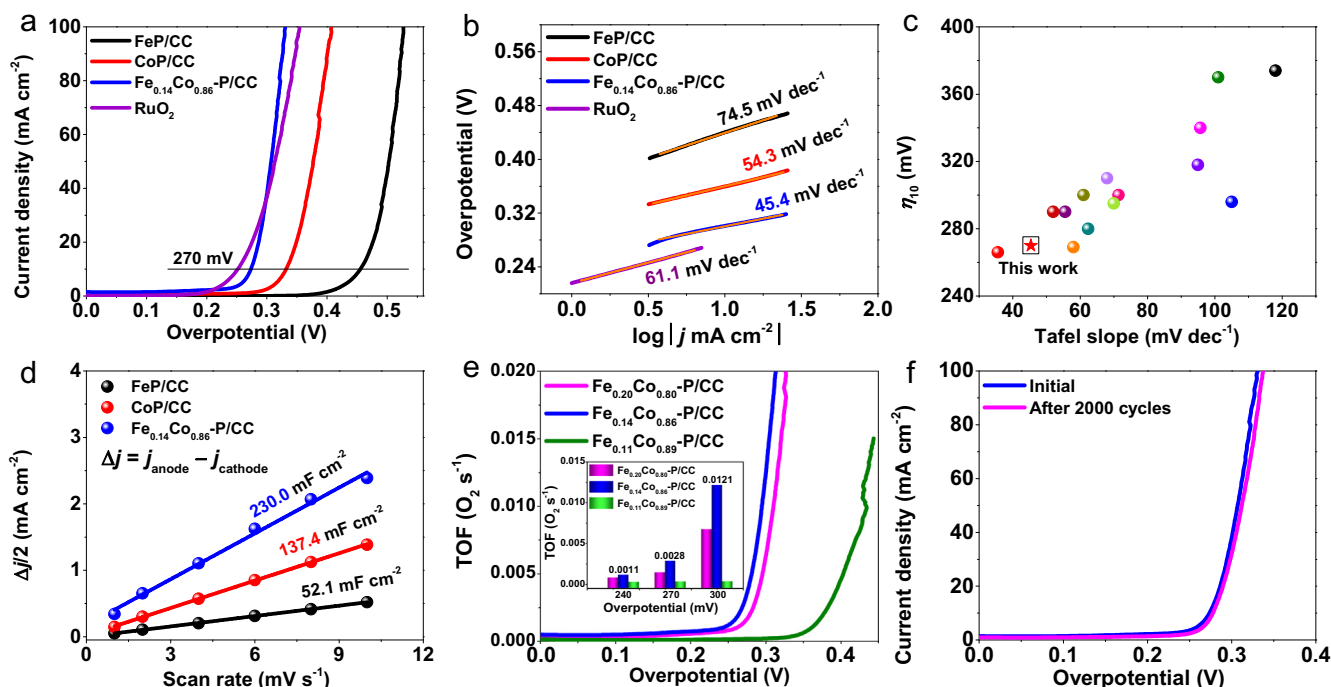


**Fig. 4.** (a) OER polarization curves of  $\text{Fe}_{0.14}\text{Co}_{0.86}\text{-P/CC}$ , together with CoP/CC, FeP/CC, and  $\text{RuO}_2\text{/CC}$  in 1.0 M KOH. (b) The corresponding Tafel slopes calculated from LSV curves from a. (c) Compared with the recently reported OER catalysts at overpotential of  $10\text{ mA cm}^{-2}$  and Tafel slope. (d) Summarized double-layer capacitance ( $C_{dl}$ ) of different catalysts. (e) The turnover frequency (TOF) profiles versus overpotential of  $\text{Fe}_{0.20}\text{Co}_{0.80}\text{-P/CC}$  (Insert: TOF values at different overpotentials). (f) Polarization curves of  $\text{Fe}_{0.14}\text{Co}_{0.86}\text{-P/CC}$  before and after 2000 cycles.

smallest  $R_{ct}$  ( $2.07 \Omega$ ) among the as-prepared precatalysts, suggesting a superior electron transfer ability and much lowered energy barrier of OER. The ultralow  $R_{ct}$  of the  $\text{Fe}_{0.14}\text{Co}_{0.86}\text{-P/CC}$  catalyst is in good agreement with the small Tafel slope and the superior OER kinetics. The LSV curves of  $\text{Fe}_{0.14}\text{Co}_{0.86}\text{-P/CC}$  remain nearly unchanged after 2000 cycles (Fig. 4f), demonstrating remarkable stability. In addition, the stability test performed at a current density of  $20 \text{ mA cm}^{-2}$  (Fig. S11) for 24 h. No obvious decline in catalytic performance was observed. However, there is a significant change in catalyst morphology (Fig. S12).

The HER performance of all catalysts was also studied in 1.0 M KOH solution. As shown in Fig. 5a, the  $\text{Fe}_{0.14}\text{Co}_{0.86}\text{-P/CC}$  catalyst displayed the best HER catalytic activity among various catalysts except commercial Pt/C. The  $\text{Fe}_{0.14}\text{Co}_{0.86}\text{-P/CC}$  catalyst can achieve a current density of  $10 \text{ mA cm}^{-2}$  at an overpotential ( $\eta_{10}$ ) of 130 mV. In comparison, the overpotentials of FeP/CC and CoP/CC are as high as 185 mV and 163 mV. The  $\text{Fe}_{0.20}\text{Co}_{0.80}\text{-P/CC}$  and  $\text{Fe}_{0.11}\text{-Co}_{0.89}\text{-P/CC}$  also require higher overpotentials of 170 mV and 270 mV respectively at  $10 \text{ mA cm}^{-2}$  (Fig. S13). Note: Commercial Pt/C needs an overpotential of 49 mV to reach  $10 \text{ mA cm}^{-2}$  under the same condition. Tafel plots were then acquired to investigate the HER kinetics [18]. The Tafel slope of  $\text{Fe}_{0.14}\text{Co}_{0.86}\text{-P/CC}$  is  $57.2 \text{ mV dec}^{-1}$ , close to that of Pt/C ( $35.5 \text{ mV dec}^{-1}$ ), but significantly lower than those of all control catalysts (Fig. 5b) as expected. The results indicate that the electrochemical desorption of hydrogen of the Volmer-Heyrovsky reaction path is the rate-determining step ( $\text{H}_2\text{O} + e^- = \text{H}_{\text{ads}} + \text{OH}^-$  and  $\text{H}_{\text{ads}} + \text{H}_2\text{O} + e^- = \text{H}_2 + \text{OH}^-$ ) [18]. Fig. 5c is a comparison graph of the overpotential at  $-10 \text{ mA cm}^{-2}$  and Tafel slope with the previously reported similar HER catalysts. It can be seen that the designed  $\text{Fe}_{0.14}\text{Co}_{0.86}\text{-P/CC}$  catalyst is obviously superior to most of these catalysts (Table S3). In addition, long-term stability is another important criterion for evaluating the practical application of electrocatalysts. Along with multicycle LSV test (Fig. 5d), we also performed chronoamperom-

etry measurement to evaluate the catalyst durability. Fig. S14 showed that  $\text{Fe}_{0.14}\text{Co}_{0.86}\text{-P/CC}$  catalyst maintained for up to 24 h at  $-10 \text{ mA cm}^{-2}$  with only a decline of about 4.1%, some of which may be associated with surface chemical state change (Fig. S6) and structural agglomeration (Fig. S15).

Industrial application of electrocatalytic water splitting is limited by massive energy penalty from uphill reaction kinetics that requires much higher voltage ( $1.8 \sim 2.4 \text{ V}$ ) than  $1.23 \text{ V}$  to reach the current density of  $200 \sim 400 \text{ mA cm}^{-2}$ . Therefore, only less than 5% of  $\text{H}_2$  is produced by electrolysis worldwide [36]. Therefore, our ultimate goal in this work is to achieve overall water splitting at a high current density and a lower voltage [17,18]. In this regard, a two electrode system of  $\text{Fe}_{0.14}\text{Co}_{0.86}\text{-P/CC}$  as both the cathode and anode for HER and OER in 30 wt% KOH electrolyte was constructed for overall water splitting (Fig. 6a), of which 30% KOH is a commonly used industrial  $\text{H}_2$  production condition by water splitting. For comparison,  $\text{RuO}_2^{+}||\text{Pt/C}^{-}$  was also examined under the same conditions. As shown in Fig. 6b, the  $\text{Fe}_{0.14}\text{Co}_{0.86}\text{-P/CC}^{(+/-)}$  could achieve the current density of  $10 \text{ mA cm}^{-2}$  at a cell voltage of 1.63 V, which is slightly higher than the benchmark  $\text{RuO}_2^{+}||\text{Pt/C}^{-}$  ( $1.57 \text{ V}$ ). It is worth noting that when the current density exceeds  $30 \text{ mA cm}^{-2}$ , the overall water splitting performance of the  $\text{Fe}_{0.14}\text{Co}_{0.86}\text{-P/CC}^{(+/-)}$  begins to surpass that of  $\text{RuO}_2^{+}||\text{Pt/C}^{-}$ . In particular, when the cell voltages are 1.95, 2.14 and 2.31 V, the current densities can reach 500, 1000 and  $1500 \text{ mA cm}^{-2}$ , respectively, showing good catalytic performance at high current density. We found that the two-electrode overall water splitting reported in this work was obviously superior to most of the previously reported works (Fig. 6c and Table S4). In addition, we used chronopotentiometry to study the stability of the catalyst. The results show that the  $\text{Fe}_{0.14}\text{Co}_{0.86}\text{-P/CC}^{(+/-)}$  electrodes can be maintained at  $10 \text{ mA cm}^{-2}$  for 48 h without any deterioration (Fig. 6d). The stability test at high current density was difficult due to the interference of large amounts of gas generated at both electrodes.

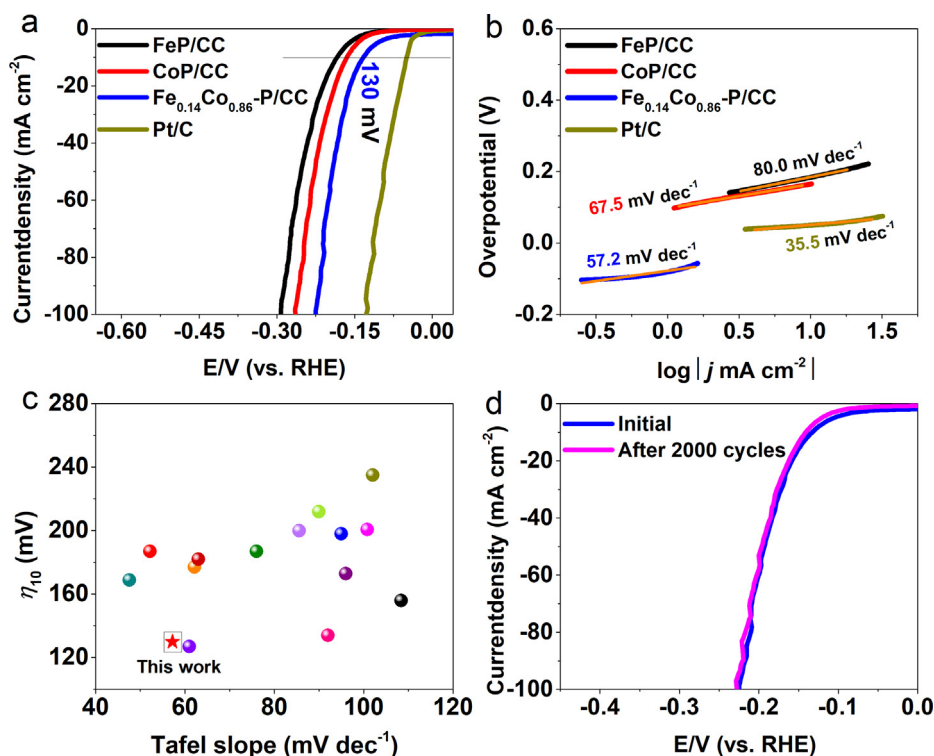


**Fig. 5.** (a) HER polarization curves of  $\text{Fe}_{0.14}\text{Co}_{0.86}\text{-P/CC}$  together with CoP/CC, FeP/CC, and Pt/C in 1.0 M KOH. (b) The corresponding Tafel slopes calculated from LSV curves in 1.0 M KOH. (c) Compare with the recently reported overpotential at  $-10 \text{ mA cm}^{-2}$  and corresponding Tafel slope of different HER catalysts (Table S3). (d) Polarization curves of  $\text{Fe}_{0.14}\text{Co}_{0.86}\text{-P/CC}$  before and after 2000 cycles.

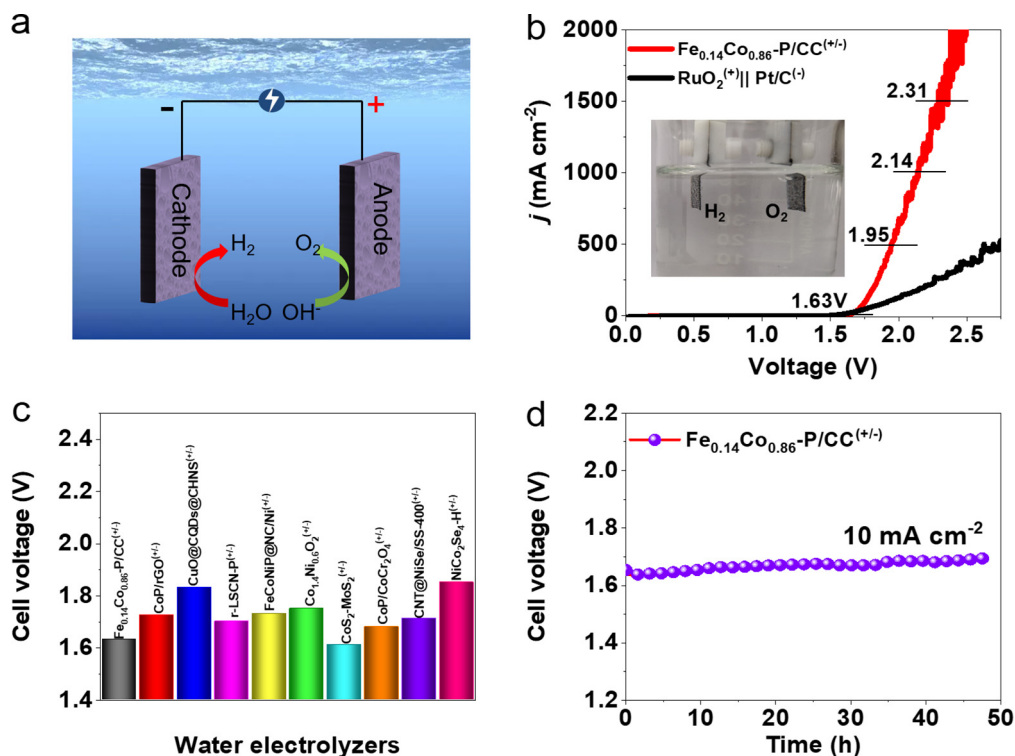


**Fig. 6.** (a) Schematic diagram of overall water splitting electrolytic cell using Fe<sub>0.14</sub>Co<sub>0.86</sub>-P/CC as both cathode and anode. (b) LSV polarization curves of the bifunctional Fe<sub>0.14</sub>Co<sub>0.86</sub>-P/CC(+/−) and RuO<sub>2</sub>(+)||Pt/C(−) for overall water splitting in 30 wt% KOH. (c) Comparing the cell voltage of the currently available electrolytic cell at 10 mA cm<sup>-2</sup> in 1.0 M KOH. (d) Chronopotentiometric curve of the bifunctional Fe<sub>0.14</sub>Co<sub>0.86</sub>-P/CC(+/−) cell at a fixed current density of 10 mA cm<sup>-2</sup> in 30 wt% KOH.

In general, the superior electrochemical activity and durability point toward the large-scale industrial applications for hydrogen production.

As discussed above, Fe<sub>0.14</sub>Co<sub>0.86</sub>-P/CC has significant OER and HER activities due to the following aspects: (1) The nanowire array structure has a larger electrochemically active surface area, which enhances the exposure of more active sites and helps electrolyte transport and gas emission [58,59]. (2) The hybrid catalyst introduced with Fe component reduces the electron transfer resistance, thereby increasing the conductivity and charge transfer. (3) The strong electronic interaction between the Fe and Co components in the catalyst optimizes the binding energy between the active site and the intermediate in the electrochemical process, thereby significantly enhancing the electrocatalytic performance [60].

#### 4. Conclusion

In summary, we have successfully synthesized Fe<sub>0.14</sub>Co<sub>0.86</sub>-P/CC nanowire array bifunctional catalyst through simple hydrothermal reaction and subsequent phosphating treatment. XPS shows that there is a strong electronic interaction between FeP and CoP components, which is beneficial to the redistribution of charges in the composite, thereby regulating the binding energy between the active site and intermediate in the electrochemical process. Electrochemical studies have found that the designed Fe<sub>0.14</sub>Co<sub>0.86</sub>-P/CC catalyst has excellent OER and HER electrocatalytic activity, small Tafel slope and good stability, which is consistent with the large electrochemical double-layer capacitance and TOF value of the catalyst. The simulated industrialized two-electrode overall water splitting study found that the bifunctional Fe<sub>0.14</sub>Co<sub>0.86</sub>-P/CC(+/−) catalyst requires smaller cell voltages to achieve high current densities (> 200 mA cm<sup>-2</sup>) combined with outstanding stability, which is apparently better than the representative RuO<sub>2</sub>(+)||Pt/C(−) catalyst under the same test conditions, showing a potential industrial prospect. These results indicate that this work can provide a valuable reference for the rational design of novel bifunctional ideal electrocatalysts for alkaline electrolyzers.

CRediT authorship contribution statement

#### CRediT authorship contribution statement

**Hongbo Yu:** Writing - original draft. **Lu Luo Qi:** Investigation, Methodology. **Yan Hu:** Data curation. **Yuan Qu:** Conceptualization. **Puxuan Yan:** Data curation, Methodology. **Tayirjan Taylor Isimjan:** Writing - review & editing. **Xiulin Yang:** Supervision, Writing - review & editing.

#### Declaration of Competing Interest

The authors declare that they have no known competing financial interests or personal relationships that could have appeared to influence the work reported in this paper.

#### Acknowledgements

This work has been supported by the National Natural Science Foundation of China (no. 21965005), Natural Science Foundation of Guangxi Province (2018GXNSFAA294077, 2021GXNSFAA076001), Project of High-Level Talents of Guangxi (F-KA18015), and Guangxi Technology Base and Talent Subject (GUIKE AD18126001, GUIKE AD20297039).

#### Appendix A. Supplementary data

Supplementary data to this article can be found online at <https://doi.org/10.1016/j.jcis.2021.05.074>.

## References

- [1] G. Luderer, M. Pehl, A. Arvesen, T. Gibon, B.L. Bodirsky, H.S. de Boer, O. Fricko, M. Hejazi, F. Humpenöder, G. Iyer, S. Mima, I. Mouratiadou, R.C. Pietzcker, A. Popp, M. van den Berg, D. van Vuuren, E.G. Hertwich, Environmental co-benefits and adverse side-effects of alternative power sector decarbonization strategies, *Nat. Commun.* 10 (2019) 5229.
- [2] J.-L. Martin, V. Maris, D.S. Simberloff, The need to respect nature and its limits challenges society and conservation science, *Proc. Nat. Acad. Sci.* 113 (2016) 6105–6112.
- [3] D. Gielen, F. Boshell, D. Saygin, M.D. Bazilian, N. Wagner, R. Gorini, The role of renewable energy in the global energy transformation, *Energy Strateg. Rev.* 24 (2019) 38–50.
- [4] S. Ott, A. Orfanidi, H. Schmies, B. Anke, H.N. Nong, J. Hubner, U. Gernert, M. Gliech, M. Lerch, P. Strasser, Ionomer distribution control in porous carbon-supported catalyst layers for high-power and low Pt-loaded proton exchange membrane fuel cells, *Nat. Mater.* 19 (2020) 77–85.
- [5] J. Zhu, M. Xiao, G. Li, S. Li, J. Zhang, G. Liu, L. Ma, T. Wu, J. Lu, A. Yu, D. Su, H. Jin, S. Wang, Z. Chen, A Triphasic Bifunctional Oxygen Electrocatalyst with Tunable and Synergetic Interfacial Structure for Rechargeable Zn-Air Batteries, *Adv. Energy Mater.* 10 (2019) 1903003.
- [6] Q. Liang, L. Zhong, C. Du, Y. Luo, J. Zhao, Y. Zheng, J. Xu, J. Ma, C. Liu, S. Li, Q. Yan, Interfacial Epitaxial Dinickel Phosphide to 2D Nickel Thiophosphate Nanosheets for Boosting Electrocatalytic Water Splitting, *ACS Nano* 13 (2019) 7975–7984.
- [7] C. Liang, P. Zou, A. Nairan, Y. Zhang, J. Liu, K. Liu, S. Hu, F. Kang, H.J. Fan, C. Yang, Exceptional performance of hierarchical Ni-Fe oxyhydroxide@NiFe alloy nanowire array electrocatalysts for large current density water splitting, *Energy Environ. Sci.* 13 (2020) 86–95.
- [8] W.H. Lai, L.F. Zhang, W.B. Hua, S. Indris, Z.C. Yan, Z. Hu, B. Zhang, Y. Liu, L. Wang, M. Liu, R. Liu, Y.X. Wang, J.Z. Wang, Z. Hu, H.K. Liu, S.L. Chou, S.X. Dou, General pi-Electron-Assisted Strategy for Ir, Pt, Ru, Pd, Fe, Ni Single-Atom Electrocatalysts with Bifunctional Active Sites for Highly Efficient Water Splitting, *Angew. Chem. Int. Ed.* 58 (2019) 11868–11873.
- [9] J.J. Duan, Z. Han, R.L. Zhang, J.J. Feng, L. Zhang, Q.L. Zhang, A.J. Wang, Iron, manganese co-doped Ni<sub>3</sub>S<sub>2</sub> nanoflowers in situ assembled by ultrathin nanosheets as a robust electrocatalyst for oxygen evolution reaction, *J. Colloid Interface Sci.* 588 (2021) 248–256.
- [10] H.-Y. Chen, H.-J. Niu, Z. Han, J.-J. Feng, H. Huang, A.-J. Wang, Simple fabrication of trimetallic platinum-nickel-cobalt hollow alloyed 3D multipods for highly boosted hydrogen evolution reaction, *J. Colloid Interface Sci.* 570 (2020) 205–211.
- [11] J.J. Duan, R.L. Zhang, J.J. Feng, L. Zhang, Q.L. Zhang, A.J. Wang, Facile synthesis of nanoflower-like phosphorus-doped Ni<sub>3</sub>S<sub>2</sub>/CoFe<sub>2</sub>O<sub>4</sub> arrays on nickel foam as a superior electrocatalyst for efficient oxygen evolution reaction, *J. Colloid Interface Sci.* 581 (2021) 774–782.
- [12] L. Li, B. Wang, G. Zhang, G. Yang, T. Yang, S. Yang, S. Yang, Electrochemically Modifying the Electronic Structure of IrO<sub>2</sub> Nanoparticles for Overall Electrochemical Water Splitting with Extensive Adaptability, *Adv. Energy Mater.* 10 (2020) 2001600.
- [13] A. Zagalskaya, V. Alexandrov, Role of Defects in the Interplay between Adsorbate Evolving and Lattice Oxygen Mechanisms of the Oxygen Evolution Reaction in RuO<sub>2</sub> and IrO<sub>2</sub>, *ACS Catal.* 10 (2020) 3650–3657.
- [14] X.K. Wan, H.B. Wu, B.Y. Guan, D. Luan, X.W.D. Lou, Confining Sub-Nanometer Pt Clusters in Hollow Mesoporous Carbon Spheres for Boosting Hydrogen Evolution Activity, *Adv. Mater.* 32 (2020) 1901349.
- [15] H. Xu, H. Shang, C. Wang, Y. Du, Surface and interface engineering of noble-metal-free electrocatalysts for efficient overall water splitting, *Coord. Chem. Rev.* 418 (2020) 213374.
- [16] H. Xu, H. Shang, C. Wang, L. Jin, C. Chen, C. Wang, Y. Du, Three-dimensional open CoMoO<sub>4</sub>/CoMoS<sub>x</sub>/CoS<sub>x</sub> nanobox electrocatalysts for efficient oxygen evolution reaction, *Appl. Catal. B: Environ.* 265 (2020) 118605.
- [17] P. Yan, M. Huang, B. Wang, Z. Wan, M. Qian, H. Yan, T.T. Isimjan, J. Tian, X. Yang, Oxygen defect-rich double-layer hierarchical porous Co<sub>3</sub>O<sub>4</sub> arrays as high-efficient oxygen evolution catalyst for overall water splitting, *J. Energy Chem.* 47 (2020) 299–306.
- [18] B. Wang, H. Huang, M. Huang, P. Yan, T.T. Isimjan, X. Yang, Electron-transfer enhanced MoO<sub>2</sub>-Ni heterostructures as a highly efficient pH-universal catalyst for hydrogen evolution, *Sci. China Chem.* 63 (2020) 841–849.
- [19] D. Zhou, S. Wang, Y. Jia, X. Xiong, H. Yang, S. Liu, J. Tang, J. Zhang, D. Liu, L. Zheng, Y. Kuang, X. Sun, B. Liu, NiFe Hydroxide Lattice Tensile Strain: Enhancement of Adsorption of Oxygenated Intermediates for Efficient Water Oxidation Catalysis, *Angew. Chem. Int. Ed.* 58 (2019) 736–740.
- [20] D. Zhou, Z. Cai, X. Lei, W. Tian, Y. Bi, Y. Jia, N. Han, T. Gao, Q. Zhang, Y. Kuang, J. Pan, X. Sun, X. Duan, NiCoFe-Layered Double Hydroxides/N-Doped Graphene Oxide Array Colloid Composite as an Efficient Bifunctional Catalyst for Oxygen Electrocatalytic Reactions, *Adv. Energy Mater.* 8 (2018) 1701905.
- [21] Q. Zhang, M. Fu, G. Ning, Y. Sun, H. Wang, X. Fan, H. Lu, Y. Zhang, H. Wang, Co/FeC core-nitrogen doped hollow carbon shell structure with tunable shell-thickness for oxygen evolution reaction, *J. Colloid Interface Sci.* 580 (2020) 794–802.
- [22] L. He, W. Zhang, Q. Mo, W. Huang, L. Yang, Q. Gao, Molybdenum Carbide-Oxide Heterostructures: in-situ Surface Reconfiguration toward Efficient Electrocatalytic Hydrogen Evolution, *Angew. Chem. Int. Ed.* 59 (2020) 3544–3548.
- [23] J.M.V. Nsanzimana, L. Gong, R. Dangol, V. Reddu, V. Jose, B.Y. Xia, Q. Yan, J.-M. Lee, X. Wang, Tailoring of Metal Boride Morphology via Anion for Efficient Water Oxidation, *Adv. Energy Mater.* 9 (2019) 1901503.
- [24] Y.R. Hong, K.M. Kim, J.H. Ryu, S. Mhin, J. Kim, G. Ali, K.Y. Chung, S. Kang, H. Han, Dual-Phase Engineering of Nickel Boride-Hydroxide Nanoparticles toward High-Performance Water Oxidation Electrocatalysts, *Adv. Funct. Mater.* 30 (2020) 2004330.
- [25] K. Jiang, M. Luo, M. Peng, Y. Yu, Y.-R. Lu, T.-S. Chan, P. Liu, F.M.F. de Groot, Y. Tan, Dynamic active-site generation of atomic iridium stabilized on nanoporous metal phosphides for water oxidation, *Nat. Commun.* 11 (2020) 2701.
- [26] X. Yang, A.-Y. Lu, Y. Zhu, M.N. Hedhili, S. Min, K.-W. Huang, Y.u. Han, L.-J. Li, CoP nanosheet assembly grown on carbon cloth: A highly efficient electrocatalyst for hydrogen generation, *Nano Energy* 15 (2015) 634–641.
- [27] W. He, L. Han, Q. Hao, X. Zheng, Y. Li, J. Zhang, C. Liu, H. Liu, H.L. Xin, Fluorine-Anion-Modulated Electron Structure of Nickel Sulfide Nanosheet Arrays for Alkaline Hydrogen Evolution, *ACS Energy Lett.* 4 (12) (2019) 2905–2912.
- [28] X. Peng, Y. Yan, X. Jin, C. Huang, W. Jin, B. Gao, P.K. Chu, Recent advance and perspectives of electrocatalysts based on transition metal selenides for efficient water splitting, *Nano Energy* 78 (2020) 105234, <https://doi.org/10.1016/j.nanoen.2020.105234>.
- [29] Z. Liu, C. Zhang, H. Liu, L. Feng, Efficient synergism of NiSe<sub>2</sub> nanoparticle/NiO nanosheet for energy-relevant water and urea electrocatalysis, *Appl. Catal. B: Environ.* 276 (2020) 119165, <https://doi.org/10.1016/j.apcatb.2020.119165>.
- [30] J. Zhang, T. Wang, D. Pohl, B. Rellinghaus, R. Dong, S. Liu, X. Zhuang, X. Feng, Interface Engineering of MoS<sub>2</sub>/Ni<sub>3</sub>S<sub>2</sub> Heterostructures for Highly Enhanced Electrochemical Overall-Water-Splitting Activity, *Angew. Chem. Int. Ed.* 55 (23) (2016) 6702–6707.
- [31] F.-T. Tsai, Y.-T. Deng, C.-W. Pao, J.-L. Chen, J.-F. Lee, K.-T. Lai, W.-F. Liaw, The HER/OER mechanistic study of an FeCoNi-based electrocatalyst for alkaline water splitting, *J. Mater. Chem. A* 8 (19) (2020) 9939–9950.
- [32] P.W. Menezes, C. Panda, C. Walter, M. Schwarze, M. Driess, A Cobalt-Based Amorphous Bifunctional Electrocatalysts for Water-Splitting Evolved from a Single-Source Lazulite Cobalt Phosphate, *Adv. Funct. Mater.* 29 (32) (2019) 1808632, <https://doi.org/10.1002/adfm.v29.3210.1002/adfm.201808632>.
- [33] H. Huang, S.i. Zhou, C. Yu, H. Huang, J. Zhao, L. Dai, J. Qiu, Rapid and Energy-Efficient Microwave Pyrolysis for High-Yield Production of Highly-Active Bifunctional Electrocatalysts for Water Splitting, *Energy Environ. Sci.* 13 (2) (2020) 545–553.
- [34] P. Liu, J.A. Rodriguez, Catalysts for Hydrogen Evolution from the [NiFe] Hydrogenase to the Ni<sub>3</sub>P(001) Surface: The Importance of Ensemble Effect, *J. Am. Chem. Soc.* 127 (2005) 14871–14878.
- [35] H. Zhang, A.W. Maijenburg, X. Li, S.L. Schweizer, R.B. Wehrspohn, Bifunctional Heterostructured Transition Metal Phosphides for Efficient Electrochemical Water Splitting, *Adv. Funct. Mater.* 30 (34) (2020) 2003261, <https://doi.org/10.1002/adfm.v30.3410.1002/adfm.202003261>.
- [36] F. Yu, H. Zhou, Y. Huang, J. Sun, F. Qin, J. Bao, W.A. Goddard, S. Chen, Z. Ren, High-performance bifunctional porous non-noble metal phosphide catalyst for overall water splitting, *Nat. Commun.* 9 (1) (2018), <https://doi.org/10.1038/s41467-018-04746-z>.
- [37] Y. Tan, H. Wang, P. Liu, Y. Shen, C. Cheng, A. Hirata, T. Fujita, Z. Tang, M. Chen, Versatile nanoporous bimetallic phosphides towards electrochemical water splitting, *Energy Environ. Sci.* 9 (7) (2016) 2257–2261.
- [38] L. Ma, S. Chen, H. Li, Z. Ruan, Z. Tang, Z. Liu, Z. Wang, Y. Huang, Z. Pei, J.A. Zapien, C. Zhi, Initiating a mild aqueous electrolyte Co<sub>3</sub>O<sub>4</sub>/Zn battery with 2.2 V-high voltage and 5000-cycle lifespan by a Co(III) rich-electrode, *Energy Environ. Sci.* 11 (2018) 2521–2530.
- [39] Zixia Wan, Hongbo Yu, Qiting He, Yan Hu, Puxuan Yan, Xue Shao, Tayirjan Taylor Isimjan, Bing Zhang, Xiulin Yang, In-situ growth and electronic structure modulation of urchin-like Ni-Fe oxyhydroxide on nickel foam as robust bifunctional catalysts for overall water splitting, *Int. J. Hydrogen Energy* 45 (43) (2020) 22427–22436.
- [40] X. Yang, A.-Y. Lu, Y. Zhu, S. Min, M.N. Hedhili, Y. Han, K.-W. Huang, L.-J. Li, Ragule-Like FeP Nanocrystal Assembly on Carbon Cloth: An Exceptionally Efficient and Stable Cathode for Hydrogen Evolution, *Nanoscale* 7 (2015) 10974–10981.
- [41] Jianrui Sun, Saisai Li, Qiaoqiao Zhang, Jingqi Guan, Iron-cobalt-nickel trimetal phosphides as high-performance electrocatalysts for overall water splitting, *Sustain. Energy. Fuels* 4 (9) (2020) 4531–4537.
- [42] Zibin Liang, Wenyang Zhou, Song Gao, Ruo Zhao, Hao Zhang, Yanqun Tang, Jinqian Cheng, Tianjie Qiu, Bingjun Zhu, Chong Qu, Wenhan Guo, Qian Wang, Ruqiang Zou, Fabrication of Hollow CoP/TiO<sub>x</sub> Heterostructures for Enhanced Oxygen Evolution Reaction, *Small* 16 (2) (2020) 1905075, <https://doi.org/10.1002/sml.v16.210.1002/sml.201905075>.
- [43] Chong Lin, Zhengfei Gao, Jianhui Yang, Bin Liu, Jian Jin, Porous superstructures constructed from ultrafine FeP nanoparticles for highly active and exceptionally stable hydrogen evolution reaction, *J. Mater. Chem. A* 6 (15) (2018) 6387–6392.
- [44] M. Qian, M. Xu, S. Zhou, J. Tian, T. Taylor Isimjan, Z. Shi, X. Yang, Template synthesis of two-dimensional ternary nickel-cobalt-nitrogen co-doped porous carbon film: promoting the conductivity and more active sites for oxygen reduction, *J. Colloid Interface Sci.* 564 (2020) 276–285.
- [45] L. Ji, L. Li, X. Ji, Y. Zhang, S. Mou, T. Wu, Q. Liu, B. Li, X. Zhu, Y. Luo, X. Shi, A.M. Asiri, X. Sun, Highly Selective Electrochemical Reduction of CO<sub>2</sub> to Alcohols on a FeP Nanoarray, *Angew. Chem. Int. Ed.* 59 (2020) 758–762.

- [46] Hui Xu, Hongyuan Shang, Liujun Jin, Chunyan Chen, Cheng Wang, Yukou Du, Boosting electrocatalytic oxygen evolution over Prussian blue analog/transition metal dichalcogenide nanoboxes by photo-induced electron transfer, *J. Mater. Chem. A* 7 (47) (2019) 26905–26910.
- [47] Yuan Pan, Kaian Sun, Shoujie Liu, Xing Cao, Konglin Wu, Weng-Chon Cheong, Zheng Chen, Yu Wang, Yang Li, Yunqi Liu, Dingsheng Wang, Qing Peng, Chen Chen, Yadong Li, Core-Shell ZIF-8@ZIF-67-Derived CoP Nanoparticle-Embedded N-Doped Carbon Nanotube Hollow Polyhedron for Efficient Overall Water Splitting, *J. Am. Chem. Soc.* 140 (7) (2018) 2610–2618.
- [48] Qianqian Sun, Zebin Yu, Ronghua Jiang, Yanping Hou, Lei Sun, Lun Qian, Fengyuan Li, Mingjie Li, Qi Ran, Heqing Zhang, CoP QD anchored carbon skeleton modified CdS nanorods as a co-catalyst for photocatalytic hydrogen production, *Nanoscale* 12 (37) (2020) 19203–19212.
- [49] K. He, T. Tadesse Tsega, X. Liu, J. Zai, X.-H. Li, X. Liu, W. Li, N. Ali, X. Qian, Utilizing the Space-charge Region of FeNi-LDH/CoP p-n Junction to Promote the Performance in Oxygen Evolution Electrocatalysis, *Angew. Chem. Int. Ed.* 58 (2019) 11903–11909.
- [50] Xu Luo, Pengxia Ji, Pengyan Wang, Ruilin Cheng, Ding Chen, Can Lin, Jianan Zhang, Jianwei He, Zuhao Shi, Neng Li, Shengqiang Xiao, Shichun Mu, Interface Engineering of Hierarchical Branched Mo-Doped Ni<sub>3</sub>S<sub>2</sub>/Ni<sub>x</sub>P<sub>y</sub> Hollow Heterostructure Nanorods for Efficient Overall Water Splitting, *Adv. Energy Mater.* 10 (17) (2020) 1903891, <https://doi.org/10.1002/aenm.v10.1710.1002/aenm.201903891>.
- [51] Yuebin Lian, Hao Sun, Xuebin Wang, Pengwei Qi, Qiaoqiao Mu, Yujie Chen, Jing Ye, Xiaohui Zhao, Zhao Deng, Yang Peng, Carved nanoframes of cobalt–iron bimetal phosphide as a bifunctional electrocatalyst for efficient overall water splitting, *Chem. Sci.* 10 (2) (2019) 464–474.
- [52] Jiahui Chen, Jianwen Liu, Jin-Qi Xie, Huangqing Ye, Xian-Zhu Fu, Rong Sun, Ching-Ping Wong, Co-Fe-P nanotubes electrocatalysts derived from metal-organic frameworks for efficient hydrogen evolution reaction under wide pH range, *Nano Energy* 56 (2019) 225–233.
- [53] Baocang Liu, Lili Huo, Zhiqing Gao, Guolei Zhi, Geng Zhang, Jun Zhang, Graphene Decorated with Uniform Ultrathin (CoP)<sub>x</sub>–(FeP)<sub>1–x</sub> Nanorods: A Robust Non-Noble-Metal Catalyst for Hydrogen Evolution, *Small* 13 (21) (2017) 1700092, <https://doi.org/10.1002/sml.v13.2110.1002/sml.201700092>.
- [54] Z. Wan, Q. He, J. Chen, T.T. Isimjan, B. Wang, X. Yang, Dissolution-regrowth of hierarchical Fe-Dy oxide modulates the electronic structure of nickel-organic frameworks as high-active and stable water splitting electrocatalysts, *Chinese J. Catal.* 41 (2020) 1745–1753.
- [55] Zixia Wan, Dandan Yang, Judan Chen, Jianniao Tian, Tayirjan Taylor Isimjan, Xiulin Yang, Oxygen-Evolution Catalysts Based on Iron-Mediated Nickel Metal–Organic Frameworks, *ACS Appl. Nano Mater.* 2 (10) (2019) 6334–6342.
- [56] Jingya Guo, Benzhi Wang, Dandan Yang, Zixia Wan, Puxuan Yan, Jianniao Tian, Tayirjan Taylor Isimjan, Xiulin Yang, Rugae-like Ni<sub>2</sub>P–CoP nanoarrays as a bifunctional catalyst for hydrogen generation: NaBH<sub>4</sub> hydrolysis and water reduction, *Appl. Catal. B: Environ.* 265 (2020) 118584, <https://doi.org/10.1016/j.apcatb.2019.118584>.
- [57] W. Yanyong, Y. Dafeng, E.H. Samir, Z. Yuqin, W. Shuangyin, Recent Progress on Layered Double Hydroxides and Their Derivatives for Electrocatalytic Water Splitting, *Adv. Sci.* 5 (2018) 1800064.
- [58] C. Dong, T. Kou, H. Gao, Z. Peng, Z. Zhang, Eutectic-Derived Mesoporous Ni-Fe-O Nanowire Network Catalyzing Oxygen Evolution and Overall Water Splitting, *Adv. Energy Mater.* 8 (2018) 1701347.
- [59] D. Lim, E. Oh, C. Lim, S.E. Shim, S.-H. Baek, Fe-doped Ni<sub>3</sub>S<sub>2</sub> nanoneedles directly grown on Ni foam as highly efficient bifunctional electrocatalysts for alkaline overall water splitting, *Electrochim. Acta* 361 (2020) 137080.
- [60] K. Jiang, S. Siahrostami, T. Zheng, Y. Hu, S. Hwang, E. Stavitski, Y. Peng, J. Dynes, M. Gangisetty, D. Su, K. Attenkofer, H. Wang, Isolated Ni single atoms in graphene nanosheets for high-performance CO<sub>2</sub> reduction, *Energy Environ. Sci.* 11 (2018) 893–903.